Acoustic-wave effects in violent bubble collapse

Thomas L. Geers,[a] Randy S. Lagumbay,[b] and Oleg V. Vasilyev[c]
Department of Mechanical Engineering, University of Colorado, Boulder, Colorado 80309, USA

(Received 29 January 2011; accepted 25 July 2012; published online 11 September 2012)

The effects of acoustic-wave propagation both outside and inside a radially collapsing and rebounding bubble are examined. This is done by comparing computational results produced by various reduced-model equations with benchmark results produced by numerical solution of the Euler equations under adiabatic conditions. Numerical inaccuracy associated with the moving bubble surface is avoided by means of a coordinate transformation that yields a fixed surface coordinate. Comparisons of calculated bubble-radius histories and peak surface pressures show that, while acoustic-wave effects in the external liquid are important, such effects in the internal gas are not. © *2012 American Institute of Physics*. [http://dx.doi.org/10.1063/1.4748870]

I. INTRODUCTION

For several decades, engineers and scientists have productively employed single-degree-of-freedom models to understand and exploit the behavior of violently collapsing bubbles [see, e.g., Leighton (1994); Young (1989, 2005); and Brenner *et al.* (2002)]. Contributions have been made by researchers and practitioners in several diverse areas: underwater explosions, cavitation damage, sonochemistry, and sonoluminescence.

The analysis of bubble dynamics extends back to the pioneering works of Besant (1859) and Rayleigh (1917), who considered the following intellectual problem: *in an infinite domain of ideal liquid under uniform pressure, a spherical volume of liquid is suddenly annihilated and the liquid rushes radially inward to close the cavity*. A more realistic problem was then considered by Lamb (1923, 1932), who filled the cavity with gas. The result was the fundamental equation of motion (fundamental EOM)

$$a\ddot{a} + \frac{3}{2}\dot{a}^2 = \bar{\rho}_\ell^{-1} P_{net}, \tag{1}$$

in which $a(t)$ is the bubble radius, $\bar{\rho}_\ell$ is the equilibrium mass density of the liquid, each overdot denotes a time derivative, and

$$P_{net}(t) = P_{gas}(t) - P_{amb}, \tag{2}$$

where $P_{gas}(t)$ is the uniform pressure in the gas and P_{amb} is the (static) ambient pressure at the bubble center in the absence of the bubble. The physical idealizations underlying Eq. (1) are: the liquid is inviscid and incompressible, and the gas has zero mass density.

In the years following the appearance of Eq. (1), numerous researchers expanded the model to include other factors, such as gas vapor pressure P_{vap}, surface tension with coefficient σ, liquid viscosity with coefficient μ, and external forcing pressure P_{for} [see, e.g., Leighton (1994), Eq. (4.81)]. With these additions,

$$P_{net} = P_{gas} + P_{vap} - P_{amb} - P_{for} - 2\sigma/a - 4\mu\dot{a}/a. \tag{3}$$

However, because our focus in this paper is on wave effects, we restrict ourselves to Eq. (2). It is a matter of some perplexity (and injustice) that Eq. (1) is widely referred to as the Rayleigh-Plesset (RP) equation, when in fact it was first published by Lamb in 1923 and included in Section 91a of the sixth edition of his famous *Hydrodynamics* (1932).

A significant limitation of Eq. (1), at least for liquids of negligible viscosity such as water, is that it does not account for the energy loss observed in experimental bubble-response data. A major step in addressing this deficiency was the incorporation of liquid compressibility and thus the admittance of acoustic radiation at collapse events. The first researcher to do this was Herring (1941), who was followed by several others [see, e.g., Kirkwood and Bethe (1942); Gilmore (1952); Keller and Kolodner (1956); Keller and Miksis (1980); and Prosperetti and Lezzi (1986)]. Of the various EOM variations, the equation of greatest interest here is the Keller and Kolodner (KK) equation

$$a\ddot{a}\left(1-\frac{\dot{a}}{\bar{c}_\ell}\right)+\frac{3}{2}\dot{a}^2\left(1-\frac{\dot{a}}{3\bar{c}_\ell}\right)=\bar{\rho}_\ell^{-1}\left[P_{net}\left(1+\frac{\dot{a}}{\bar{c}_\ell}\right)+\frac{a}{\bar{c}_\ell}\dot{P}_{net}\right], \tag{4}$$

where $\bar{c}_\ell$ is the speed of sound in the liquid for moderate adiabatic compression and expansion about the equilibrium state. The essential mathematical difference between this equation and Eq. (1) is that the velocity potential in the liquid is taken as satisfying the wave equation rather than Laplace's equation.

Now it is to be expected that, if acoustic waves are launched in the liquid at collapse events, similar waves would simultaneously be launched in the gas. However, this was apparently not considered until 2000, when Moss *et al.* modified the EOM of Löfstedt *et al.* (1993). The result was the MLS equation

$$a\ddot{a}+\frac{3}{2}\dot{a}^2=\bar{\rho}_\ell^{-1}\left[P_{net}+\frac{a}{\bar{c}_\ell}\dot{P}_{net}+\frac{a}{3c_g}\dot{P}_{gas}+\frac{a}{3\bar{c}_\ell}\frac{d}{dt}\left(\frac{a}{c_g}\dot{P}_{gas}\right)\right], \tag{5}$$

where $c_g(t)$ is the spatially uniform speed of sound in the gas. Unfortunately, when the terms containing c_g are dropped

[a]thomas.geers@colorado.edu.
[b]randy.lagumbay@colorado.edu.
[c]oleg.vasilyev@colorado.edu.

from this equation, one obtains an EOM that is not consistent with Eq. (4) through order $\dot{a}/\bar{c}_\ell$. And because (4) possesses such consistency with the EOM of Herring (1941), Kirkwood and Bethe (1942), Gilmore (1952) (when simplified), and Prosperetti and Lezzi (1986), it appears that Eq. (5) is the odd man out. However, numerical computations have shown this to be a matter of minor significance.

A second treatment of acoustic-wave generation in both the liquid and the gas was presented by Geers and Hunter in 2002. Their formulation considered general bubble motion, and employed first-order doubly asymptotic approximations (DAAs) for both the external liquid and the internal gas [Geers and Zhang (1994)]. When specialized to the dilating bubble, this produced the GH equation

$$\begin{aligned} &a\ddot{a}\left[1-\left(1-\frac{\rho_g}{\bar{\rho}_\ell}\right)\frac{\dot{a}}{\bar{c}_\ell}+\zeta\right] \\ &+\frac{3}{2}\dot{a}^2\left[1-\frac{\dot{a}}{3\bar{c}_\ell}+\frac{2}{3}\zeta+\frac{1}{3}\left(\frac{\rho_g}{\bar{\rho}_\ell}\right)\left(1+\frac{\dot{a}}{\bar{c}_\ell}+\frac{a}{\bar{c}_\ell}\cdot\frac{\dot{\rho}_g}{\rho_g}\right)\right] \\ &+\left(\zeta\bar{c}_\ell+\dot{\zeta}a\right)\dot{a}=\bar{\rho}_\ell^{-1}\left[P_{net}\left(1+\frac{\dot{a}}{\bar{c}_\ell}\right)+\frac{a}{\bar{c}_\ell}\dot{P}_{net}\right], \end{aligned} \tag{6}$$

where $\zeta(t)=\rho_g(t)c_g(t)/\bar{\rho}_\ell\bar{c}_\ell$ is the ratio of the specific acoustic impedance of the gas to that of the liquid. If ρ_g is set to zero in Eq. (6), the result is Eq. (4), which is to be expected, as the external DAA_1 is exact for small-motion dilation of a spherical surface in an infinite acoustic medium.

A third treatment of acoustic-wave generation in both the liquid and the gas was formulated by Lin *et al.* (2002). They examined non-uniform fields in the gas bubble linked to bubble-surface acceleration, obtaining the LSS equation

$$\begin{aligned} &\frac{1}{2}\frac{\rho_g}{\bar{\rho}_\ell}\frac{a^2}{\bar{c}_\ell}\dddot{a}+a\ddot{a}\left[1-2\frac{\dot{a}}{\bar{c}_\ell}+\frac{1}{2}\frac{\rho_g}{\bar{\rho}_\ell}\left(1+\frac{\dot{a}}{\bar{c}_\ell}\right)\right] \\ &+\frac{3}{2}\dot{a}^2\left(1-\frac{4}{3}\frac{\dot{a}}{\bar{c}_\ell}\right)=\bar{\rho}_\ell^{-1}\left(P_{net}+\frac{a}{\bar{c}_\ell}\dot{P}_{net}\right). \end{aligned} \tag{7}$$

This ordinary differential equation is one order higher than the preceding EOM, requiring an initial value for $\ddot{a}$; this value is readily obtained from Eq. (1) expressed at $t=0$.

In this paper, we examine the significance of acoustic-wave effects in the gas relative to those in the liquid. This is done by comparing numerical results produced by Eqs. (1) and (4)–(7) with benchmark results for a specially designed problem. The problem is one with initial conditions that launch purely incompressible flow so that all of the responses start precisely together. Because the inclusion of other phenomena such as heat and mass transfer, chemical dissociation, and light emission would do nothing but cloud the comparisons, simple adiabatic compression and expansion is assumed throughout.

The benchmark results are produced by finite-difference discretization of the Euler equations for both the gas and the liquid. Numerical artifacts in the benchmark results are minimized by a transformation of coordinates that yields a stationary bubble surface, which avoids the numerical inaccuracies associated with a moving boundary. In addition, the resulting two-field problem with a stationary boundary is reduced to a single-field problem with parameters that change at that boundary.

II. EOM FOR ADIABATIC CONDITIONS

As stated above, we employ an adiabatic compression and expansion model for the bubble gas, i.e., $P_{gas}=P_{amb}(\bar{a}/a)^{3\gamma}$, where $\bar{a}$ is the equilibrium radius and γ is the ratio of specific heats. Conservation of mass in the gas bubble yields $\rho_g=\bar{\rho}_g(\bar{a}/a)^3$, where $\bar{\rho}_g$ is the gas density at equilibrium. The bulk-modulus relations $B_g=\rho_g c_g^2$ and $B_g=-\Delta P_{gas}/(\Delta Vol./Vol.)$ then yield $c_g=\bar{c}_g(\bar{a}/a)^{3(\gamma-1)/2}$, where $\bar{c}_g=\sqrt{\gamma P_{amb}/\bar{\rho}_g}$. Thus, $\zeta=\left(\bar{\rho}_g\bar{c}_g/\bar{\rho}_\ell\bar{c}_\ell\right)(\bar{a}/a)^{3(\gamma+1)/2}$.

Employing the adiabatic model in Eq. (2), we obtain from Eq. (1)

$$a\ddot{a}+\frac{3}{2}\dot{a}^2+\bar{\rho}_\ell^{-1}P_{amb}\left[1-(\bar{a}/a)^{3\gamma}\right]=0, \tag{8}$$

and from Eq. (4)

$$\begin{aligned} &a\ddot{a}\left(1-\frac{\dot{a}}{\bar{c}_\ell}\right)+\frac{3}{2}\dot{a}^2\left(1-\frac{\dot{a}}{3\bar{c}_\ell}\right)+\frac{P_{amb}}{\bar{\rho}_\ell\bar{c}_\ell}\left[1+(3\gamma-1)(\bar{a}/a)^{3\gamma}\right]\dot{a} \\ &+\bar{\rho}_\ell^{-1}P_{amb}\left[1-(\bar{a}/a)^{3\gamma}\right]=0. \end{aligned} \tag{9}$$

Similarly, Eq. (5) yields

$$\begin{aligned} &a\ddot{a}\left[1+\frac{\gamma P_{amb}}{\bar{\rho}_\ell\bar{c}_\ell\bar{c}_g}(\bar{a}/a)^{3(\gamma+1)/2}\right] \\ &+\frac{3}{2}\dot{a}^2\left[1-\frac{\gamma(\gamma+1)}{\bar{\rho}_\ell\bar{c}_\ell\bar{c}_g}P_{amb}(\bar{a}/a)^{3(\gamma+1)/2}\right] \\ &+\frac{3\gamma}{\bar{\rho}_\ell\bar{c}_\ell}P_{amb}(\bar{a}/a)^{3\gamma}\left[1+\frac{\bar{c}_\ell}{3\bar{c}_g}(a/\bar{a})^{3(\gamma-1)/2}\right]\dot{a} \\ &+\bar{\rho}_\ell^{-1}P_{amb}\left[1-(\bar{a}/a)^{3\gamma}\right]=0, \end{aligned} \tag{10}$$

and Eq. (6) produces

$$\begin{aligned} &a\ddot{a}\left[1+\zeta-\left(1-\frac{\rho_g}{\bar{\rho}_\ell}\right)\frac{\dot{a}}{\bar{c}_\ell}\right] \\ &+\frac{3}{2}\dot{a}^2\left[1-\frac{\dot{a}}{3\bar{c}_\ell}+\frac{2}{3}\zeta+\frac{\rho_g}{3\bar{\rho}_\ell}\left(1+\frac{\dot{a}}{\bar{c}_\ell}+\frac{a}{\bar{c}_\ell}\cdot\frac{\dot{\rho}_g}{\rho_g}\right)\right] \\ &+\left\{\frac{P_{amb}}{\bar{\rho}_\ell\bar{c}_\ell}\left[1+(3\gamma-1)(\bar{a}/a)^{3\gamma}\right]+\zeta\bar{c}_\ell+\dot{\zeta}a\right\}\dot{a} \\ &+\bar{\rho}_\ell^{-1}P_{amb}\left[1-(\bar{a}/a)^{3\gamma}\right]=0. \end{aligned} \tag{11}$$

Finally, Eq. (7) becomes for the adiabatic model

$$\begin{aligned} &\frac{1}{2}\left(\frac{\bar{\rho}_g}{\bar{\rho}_\ell}\right)\frac{\bar{a}^3}{\bar{c}_\ell}a^{-1}\dddot{a}+a\ddot{a}\left[1-2\frac{\dot{a}}{\bar{c}_\ell}+\frac{1}{2}\frac{\bar{\rho}_g}{\bar{\rho}_\ell}\left(\frac{\bar{a}}{a}\right)^3\left(1+\frac{\dot{a}}{\bar{c}_\ell}\right)\right] \\ &+\frac{3}{2}\dot{a}^2\left(1-\frac{4\dot{a}}{3\bar{c}_\ell}\right)+\frac{3\gamma}{\bar{\rho}_\ell\bar{c}_\ell}P_{amb}(\bar{a}/a)^{3\gamma}\dot{a} \\ &+\bar{\rho}_\ell^{-1}P_{amb}\left[1-(\bar{a}/a)^{3\gamma}\right]=0. \end{aligned} \tag{12}$$

III. BENCHMARK PROBLEM

A spherical bubble at equilibrium has been slowly expanded radially and adiabatically to an initial radius substantially greater than its equilibrium radius $\bar{a}$, which has decreased the uniform pressure in the gas to nearly zero. In addition, a pressure field exists in the surrounding liquid that varies as $1/r$. At $t=0$, the bubble surface is suddenly released and the surrounding liquid flows radially inward, past the original equilibrium position, until the internal gas becomes sufficiently pressurized to reverse the motion. The abrupt reversal generates acoustic waves that propagate outward through the surrounding liquid and inward through the bubble gas.

The acoustic energy in the outward-propagating wave is, of course, radiated away, but the acoustic energy in the inward-propagating wave is apparently not lost. However, each impingement of an internal wave on the inner surface of the bubble produces transmission of acoustic energy into the liquid, which may then be radiated outward. Because of the large impedance mismatch between the gas and the liquid ($\zeta \ll 1$), energy transmission at each impingement is small.

The rebound of the bubble produces outward flow of the liquid until the bubble surface reaches a maximum radius somewhat smaller than the initial radius. At this point, inward flow resumes, eventually leading to another abrupt flow reversal with the concomitant generation of acoustic waves. This pattern is repeated through many cycles until the bubble settles down to its equilibrium radius. Because the time between abrupt bubble reversals greatly exceeds the time required for an acoustic disturbance in the gas to cross the bubble, numerous internal acoustic impingements occur between abrupt reversals.

IV. EULER-EQUATION (EE) FORMULATION

The continuity and momentum equations for both the external liquid and the internal gas are

$$\begin{aligned} &\frac{\partial \rho}{\partial t}+\frac{\partial}{\partial r}(\rho u)+\frac{2}{r}\rho u=0,\\ &\rho\left(\frac{\partial u}{\partial t}+u\frac{\partial u}{\partial r}\right)+\frac{\partial p^*}{\partial r}=0, \end{aligned} \tag{13}$$

where $\rho(r,t)$, $u(r,t)$, and $p^*(r,t)$ are, respectively, mass density, radial velocity, and gauge pressure $p^*(r,t)=p(r,t)-P_{amb}$. Although Eqs. (13) are the same for the liquid and the gas, their equations of state are quite different.

For the liquid, we employ the linearized equation of state

$$p_\ell^* = \bar{c}_\ell{}^2 \rho_\ell^*, \tag{14}$$

where $\rho_\ell^*(r,t)=\rho_\ell(r,t)-\bar{\rho}_\ell$. Then we use this and Eq. (14) in Eq. (13) and exploit the fact that $\rho_\ell^* \ll \bar{\rho}_\ell$ to obtain the desired pressure-velocity equations for the liquid

$$\begin{aligned} &\frac{\partial p_\ell^*}{\partial t}+u_\ell\frac{\partial p_\ell^*}{\partial r}+\bar{\rho}_\ell\bar{c}_\ell{}^2\left(\frac{\partial u_\ell}{\partial r}+\frac{2}{r}u_\ell\right)=0,\\ &\frac{\partial p_\ell^*}{\partial r}+\bar{\rho}_\ell\left(\frac{\partial u_\ell}{\partial t}+u_\ell\frac{\partial u_\ell}{\partial r}\right)=0. \end{aligned} \tag{15}$$

For the gas, we employ the adiabatic equation of state

$$\rho_g = \bar{\rho}_g (p_g/P_{amb})^{1/\gamma} \tag{16}$$

along with $p_g(r,t)=p_g^*(r,t)+P_{amb}$ to obtain

$$\begin{aligned} \frac{\partial \rho_g}{\partial t} &= \frac{\bar{\rho}_g}{\gamma\left(p_g^*+P_{amb}\right)}\left(\frac{p_g^*+P_{amb}}{P_{amb}}\right)^{1/\gamma}\frac{\partial p_g^*}{\partial t},\\ \frac{\partial \rho_g}{\partial r} &= \frac{\bar{\rho}_g}{\gamma\left(p_g^*+P_{amb}\right)}\left(\frac{p_g^*+P_{amb}}{P_{amb}}\right)^{1/\gamma}\frac{\partial p_g^*}{\partial r}. \end{aligned} \tag{17}$$

Then we introduce these into Eq. (13) to obtain the desired pressure-velocity equations for the gas

$$\begin{aligned} &\frac{\partial p_g^*}{\partial t}+u_g\frac{\partial p_g^*}{\partial r}+\gamma\left(p_g^*+P_{amb}\right)\left(\frac{\partial u_g}{\partial r}+\frac{2}{r}u_g\right)=0,\\ &\frac{\partial p_g^*}{\partial r}+\bar{\rho}_g\left(\frac{p_g^*+P_{amb}}{P_{amb}}\right)^{1/\gamma}\left(\frac{\partial u_g}{\partial t}+u_g\frac{\partial u_g}{\partial r}\right)=0. \end{aligned} \tag{18}$$

V. BOUNDARY AND INITIAL CONDITIONS

At the center of the bubble, we have the essential boundary condition

$$u_g(0,t)=0. \tag{19}$$

The essential and natural boundary conditions at the bubble surface are simply

$$u_g(a,t)=u_\ell(a,t)=u(a,t), \quad p_g^*(a,t)=p_\ell^*(a,t), \tag{20}$$

in which the bubble surface is defined by

$$a(t)=\alpha\bar{a}+\int_0^t u(a,t')dt', \tag{21}$$

where α is the ratio of the initial radius to the equilibrium radius.

The computational domain is bounded by the external first-order DAA boundary [Geers and Hunter, 2002]

$$\frac{\partial \phi_\ell}{\partial r}(R,t)=-\frac{1}{R}\phi_\ell(R,t)-\frac{1}{\bar{c}_\ell}\frac{\partial \phi_\ell}{\partial t}(R,t), \tag{22}$$

where $\phi_\ell(r,t)$ is the velocity potential for the liquid and $R \geq \alpha\bar{a}$. In the limit $R\to\infty$, Eq. (22) becomes the Sommerfeld radiation condition [see, e.g., Pierce (1989)]. Now

$$u_\ell(r,t)=\frac{\partial \phi_\ell}{\partial r}(r,t), \quad p_\ell^*(r,t)=-\bar{\rho}_\ell\left[\frac{\partial \phi_\ell}{\partial t}(r,t)+\frac{1}{2}u_\ell^2(r,t)\right], \tag{23}$$

so $\bar{\rho}_\ell\bar{c}_\ell\frac{\partial}{\partial t}$ Eq. (22) yields the pressure-velocity boundary

$$\begin{aligned} &\frac{\partial p_\ell^*}{\partial t}(R,t)+\frac{\bar{c}_\ell}{R}p_\ell^*(R,t)\\ &\quad=\bar{\rho}_\ell\bar{c}_\ell\left\{\left[1-u_\ell(R,t)/\bar{c}_\ell\right]\frac{\partial u_\ell}{\partial t}(R,t)-\frac{1}{2R}u_\ell^2(R,t)\right\}. \end{aligned} \tag{24}$$

Now the initial conditions for the gas are

$$u_g(r,0)=0, \quad p_g(r,0)=P_g, \tag{25}$$

where P_g is the result of the gas having been expanded slowly and adiabatically from the equilibrium volume to the initial volume. Because the density of the gas is uniform in both cases, conservation of mass yields $\rho_g(r,0)=\alpha^{-3}\bar{\rho}_g$. Thus, from Eq. (16), $P_g=\alpha^{-3\gamma}P_{amb}$ and so, with $p_g^*(r,0)=P_g-P_{amb}$,

$$p_g^*(r,0)=-(1-\alpha^{-3\gamma})P_{amb}. \tag{26}$$

The initial conditions for the liquid are

$$u_\ell(r,0)=0, \quad p_\ell^*(r,0)=p_g^*(r,0)\frac{\alpha\bar{a}}{r}. \tag{27}$$

The latter establishes continuity of pressure at the bubble surface and initiates an incompressible-flow field in the liquid.

VI. SINGLE-FIELD EQUATIONS

Equations (15), (18), and (20) admit a single-field representation of the benchmark problem. The domain equations are

$$\begin{aligned}&\frac{\partial p^*}{\partial t}+u\frac{\partial p^*}{\partial r}+B\left(\frac{\partial u}{\partial r}+\frac{2}{r}u\right)=0,\\&\frac{\partial p^*}{\partial r}+D\left(\frac{\partial u}{\partial t}+u\frac{\partial u}{\partial r}\right)=0,\end{aligned} \tag{28}$$

where the bulk-modulus and density coefficients are

$$\begin{aligned}B&=\begin{cases}\gamma P_{amb}(1+p_g^*/P_{amb}),\ 0\le r<a\\ \bar{\rho}_\ell\bar{c}_\ell^2,\ a<r\le R\end{cases},\\ D&=\begin{cases}\bar{\rho}_g(1+p_g^*/P_{amb})^{1/\gamma},\ 0\le r<a\\ \bar{\rho}_\ell,\ a<r\le R\end{cases}.\end{aligned} \tag{29}$$

The boundary equations are, from Eqs. (19) and (24),

$$\begin{aligned}u(0,t)=0, \quad &\frac{\partial p^*}{\partial t}(R,t)+\frac{\bar{c}_\ell}{R}p^*(R,t)\\&=\bar{\rho}_\ell\bar{c}_\ell\left\{[1-u(R,t)/\bar{c}_\ell]\frac{\partial u}{\partial t}(R,t)-\frac{1}{2R}u^2(R,t)\right\},\end{aligned} \tag{30}$$

and the initial conditions are, from Eqs. (25)–(27),

$$\begin{aligned}&u(r,0)=0,\\&p^*(r,0)=\begin{cases}-(1-\alpha^{-3\gamma})P_{amb},\ 0\le r\le\alpha\bar{a}\\ -(1-\alpha^{-3\gamma})P_{amb}\alpha\bar{a}/r,\ \alpha\bar{a}\le r\le R\end{cases}.\end{aligned} \tag{31}$$

VII. TRANSFORMATION OF COORDINATES

To obtain a numerical solution that maintains a sharp boundary between the liquid and the gas, we introduce the following coordinate transformation:

$$\eta=r/a(t), \quad \tau=t. \tag{32}$$

Hence, for any continuous function $f(r,t)$,

$$\begin{aligned}\frac{\partial f}{\partial r}&=\frac{\partial f}{\partial\eta}\frac{\partial\eta}{\partial r}+\frac{\partial f}{\partial\tau}\frac{\partial\tau}{\partial r}=\frac{1}{a(t)}\frac{\partial f}{\partial\eta},\\ \frac{\partial f}{\partial t}&=\frac{\partial f}{\partial\tau}\frac{\partial\tau}{\partial t}+\frac{\partial f}{\partial\eta}\frac{\partial\eta}{\partial t}=\frac{\partial f}{\partial\tau}-\eta\frac{\dot{a}(\tau)}{a(\tau)}\frac{\partial f}{\partial\eta}.\end{aligned} \tag{33}$$

Applying Eqs. (32) and (33) to Eqs. (28), we obtain the following equations for $p^*(\eta,\tau)$ and $u(\eta,\tau)$:

$$\begin{aligned}\frac{\partial p^*}{\partial\tau}&=-\frac{1}{a}\left[(u-\eta\dot{a})\frac{\partial p^*}{\partial\eta}+B\left(\frac{\partial u}{\partial\eta}+\frac{2}{\eta}u\right)\right],\\ \frac{\partial u}{\partial\tau}&=\frac{1}{a}\left[(\eta\dot{a}-u)\frac{\partial u}{\partial\eta}-\frac{1}{D}\frac{\partial p^*}{\partial\eta}\right],\end{aligned} \tag{34}$$

in which, from Eqs. (21) and (29),

$$\begin{aligned}a(\tau)&=\alpha\bar{a}+\int_0^\tau u(1,\tau')d\tau',\\ B&=\begin{cases}\gamma P_{amb}(1+p_g^*/P_{amb}),\ 0\le\eta<1\\ \bar{\rho}_\ell\bar{c}_\ell^2,\ 1<\eta\le\beta\end{cases},\\ D&=\begin{cases}\bar{\rho}_g(1+p_g^*/P_{amb})^{1/\gamma},\ 0\le\eta<1\\ \bar{\rho}_\ell,\ 1<\eta\le\beta\end{cases},\end{aligned} \tag{35}$$

where $\beta=R/a\ge1$. Applying Eqs. (32) and (33) to Eqs. (30) and (31), we get the boundary and initial conditions

$$\begin{aligned}u(0,\tau)=0, \quad &\frac{\partial p^*}{\partial\tau}(\beta,\tau)-\beta\frac{\dot{a}(\tau)}{a(\tau)}\frac{\partial p^*}{\partial\eta}(\beta,\tau)+\frac{\bar{c}_\ell}{\beta a(\tau)}p^*(\beta,\tau)\\&=\bar{\rho}_\ell\bar{c}_\ell\left\{[1-u(\beta,\tau)/\bar{c}_\ell]\left[\frac{\partial u}{\partial\tau}(\beta,\tau)-\beta\frac{\dot{a}(\tau)}{a(\tau)}\frac{\partial u}{\partial\eta}(\beta,\tau)\right]\right.\\&\left.-\frac{1}{2\beta a(\tau)}u^2(\beta,\tau)\right\},\end{aligned} \tag{36}$$

$$u(\eta,0)=0, \quad p^*(\eta,0)=\begin{cases}-(1-\alpha^{-3\gamma})P_{amb},\ 0\le\eta\le1\\ -(1-\alpha^{-3\gamma})P_{amb}/\eta,\ 1\le\eta\le\beta.\end{cases} \tag{37}$$

It is interesting to note that a fixed value of β means that R is proportional to $a(t)$, i.e., that the computational boundary in physical space is a moving one. This is no cause for concern because the second of (30) holds at any $R\ge a$.

VIII. NUMERICAL METHOD

We spatially discretize the pressure and velocity fields with the staggered-grid central-difference method [Fletcher (1988)]. Pressures $p_i^*(\tau)$, $i=1,2,\ldots,J$, are calculated at the centers of computational cells of uniform length, and corresponding velocities $u_{i-1/2}(\tau)$, $u_{i+1/2}(\tau)$ are calculated at the cell boundaries. Derivatives are approximated as

$$\begin{aligned}\left[\frac{\partial p^*}{\partial\eta}\right]_i&=\frac{p_{i+1}^*-p_{i-1}^*}{\eta_{i+1}-\eta_{i-1}}, \quad \left[\frac{\partial u}{\partial\eta}\right]_i=\frac{u_{i+1/2}-u_{i-1/2}}{\eta_{i+1/2}-\eta_{i-1/2}},\\ \left[\frac{\partial p^*}{\partial\eta}\right]_{i+1/2}&=\frac{p_{i+1}^*-p_i^*}{\eta_{i+1}-\eta_i}, \quad \left[\frac{\partial u}{\partial\eta}\right]_{i+1/2}=\frac{u_{i+3/2}-u_{i-1/2}}{\eta_{i+3/2}-\eta_{i-1/2}},\end{aligned} \tag{38}$$

where $\eta_i=\left(i-\frac{1}{2}\right)\Delta\eta$ and $\eta_{i+1}-\eta_i=\eta_{i+1/2}-\eta_{i-1/2}=\Delta\eta$. The bubble center is located at $\eta_{1/2}$, the bubble surface at

$\eta_{I+1/2}$, and the last point in the computational mesh at $\eta_{J+1/2}$. The following formulas are also used:

$$\left[\frac{\partial p^*}{\partial \eta}\right]_J = \frac{p_J^* - p_{J-1}^*}{\eta_J - \eta_{J-1}}, \quad u_i = \frac{1}{2}\left(u_{i+1/2} + u_{i-1/2}\right),$$
$$D_{i+1/2} = \begin{cases} \frac{1}{2}(D_i + D_{i+1}), \ i \neq I \\ \varphi_g D_I + \varphi_\ell D_{I+1}, \ i = I \end{cases}, \tag{39}$$

where the volume fractions φ_g and φ_ℓ are given by

$$\varphi_g = \frac{\eta_{I+1/2}^3 - \eta_I^3}{\eta_{I+1}^3 - \eta_I^3}, \quad \varphi_\ell = \frac{\eta_{I+1}^3 - \eta_{I+1/2}^3}{\eta_{I+1}^3 - \eta_I^3}. \tag{40}$$

We solve the first of Eqs. (34) at the cell centers and the second of Eqs. (34) at the cell boundaries. The introduction of Eqs. (38) and (39) then yields

$$\left[\frac{\partial p^*}{\partial \tau}\right]_i = -\frac{1}{a}\left[\frac{1}{2}\left(u_{i+1/2} + u_{i-1/2}\right) - \eta_i \dot{a}\right]\frac{p_{i+1}^* - p_{i-1}^*}{\eta_{i+1} - \eta_{i-1}} - \frac{B_i}{a}\left[\frac{u_{i+1/2} - u_{i-1/2}}{\eta_{i+1/2} - \eta_{i-1/2}} + \frac{1}{\eta_i}\left(u_{i+1/2} + u_{i-1/2}\right)\right],$$
$$\left[\frac{\partial u}{\partial \tau}\right]_{i+1/2} = -\frac{1}{a}\left[\left(u_{i+1/2} - \eta_{i+1/2}\dot{a}\right)\frac{u_{i+3/2} - u_{i-1/2}}{\eta_{i+3/2} - \eta_{i-1/2}} + \frac{1}{D_{i+1/2}}\frac{p_{i+1}^* - p_i^*}{\eta_{i+1} - \eta_i}\right], \tag{41}$$

where $D_{i+1/2}$ is given in Eqs. (39) and, from Eqs. (35),

$$a(\tau) = \alpha\bar{a} + \int_0^\tau u_{I+1/2}(\tau')d\tau',$$
$$B_i = \begin{cases} \gamma P_{amb}(1 + p_i^*/P_{amb}), \ 1 \le i \le I \\ \bar{\rho}_\ell \bar{c}_\ell^2, \ I+1 \le i \le J \end{cases}, \tag{42}$$
$$D_i = \begin{cases} \bar{P}_g(1 + p_i^*/P_{amb})^{1/\gamma}, \ 1 \le i \le I \\ \bar{\rho}_\ell, \ I+1 \le i \le J \end{cases}.$$

The end conditions at the bubble center ($\eta_{1/2}$) are, from the first of Eqs. (36) and the requirement of zero slope in pressure,

$$u_{1/2}(\tau) = 0, \quad p_0^*(\tau) = p_1^*(\tau), \tag{43}$$

and, from the second of Eqs. (36), the end condition at the outermost pressure node ($i = J$) is

$$\frac{\partial p_J^*}{\partial \tau} - \eta_J\left(\frac{\dot{a}}{a}\right)\frac{p_J^* - p_{J-1}^*}{\eta_J - \eta_{J-1}} + \frac{\bar{c}_\ell}{\eta_J a}p_J^*$$
$$= \bar{\rho}_\ell \bar{c}_\ell\left\{\left[1 - \frac{1}{2}\left(u_{J+1/2} + u_{J-1/2}\right)/\bar{c}_\ell\right]\right.$$
$$\times\left[\frac{\partial u_J}{\partial \tau} - \eta_J\left(\frac{\dot{a}}{a}\right)\frac{u_{J+1/2} - u_{J-1/2}}{\eta_{J+1/2} - \eta_{J-1/2}}\right]$$
$$\left. - \frac{1}{8\eta_J a}\left(u_{J+1/2} + u_{J-1/2}\right)^2\right\}. \tag{44}$$

Equations (41) and (44) are integrated numerically with a fourth-order Runge-Kutta scheme.

IX. COMPUTATIONAL RESULTS

The initial computational task is to assess the accuracy of the baseline EE model that generates the benchmark results; the model is characterized by $\Delta\eta = 0.83 \times 10^{-2}$, $\beta = 7$, and $\Delta\hat{t} = 3.16\times10^{-4}$, in which $\Delta\hat{t} = \Delta t/\bar{t}$, where $\bar{t} = \bar{a}/\sqrt{P_{amb}/\bar{\rho}_\ell}$.

First, we compare EE-computed bubble-radius histories for various locations of the DAA boundary. Histories produced with $\alpha = 3$, $\Delta\eta = 0.83 \times 10^{-2}$, and $\Delta\hat{t} = 3.16\times10^{-4}$ for $\beta = 3,5,7,9$ are shown in Figure 1. The four histories appear coincident. Tabulated in Table I are normalized RMS errors in the bubble-radius histories, defined by

$$\varepsilon_a(\beta, 9) = \left\{\frac{\int_0^{10\hat{t}}[a_\beta(t) - a_9(t)]^2 dt}{\int_0^{10\hat{t}}[a_9(t)]^2 dt}\right\}^{1/2} \times 100\%, \tag{45}$$

where the a-subscripts denote β-values. The error for $\beta = 7$ is extremely small. Even the error for $\beta = 3$ (which places the computational boundary on the bubble surface) is less than 1%, so the DAA boundary is very effective.

Surface-pressure histories over the duration $0 \le t/\bar{t} \le 10$ for $\beta = 3,5,7,9$ appear as nearly identical spikes occurring at the times of bubble collapse, which is not very illuminating. Better understanding may be gained from Figure 2, which pertains to the first bubble collapse during $2.755 \le t/\bar{t} \le 2.785$. Furthermore, because RMS error is excessively

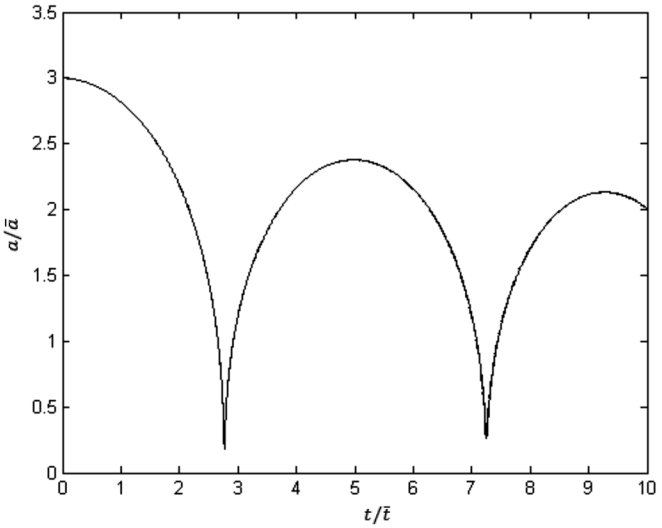

FIG. 1. EE bubble-radius histories computed with $\alpha = 3$, $\Delta\eta = 0.0083$, $\Delta\hat{t} = 3.16 \times 10^{-4}$, and $\beta = 3,5,7,9$.

TABLE I. Normalized RMS bubble-radius errors and peak-pressure errors during $0 \le t/\bar{t} \le 10$ for $\alpha = 3$, $\Delta\eta = 0.83\times10^{-2}$, $\Delta\hat{t} = 3.16\times10^{-4}$, and three values of β for EE calculations with the corresponding bubble-radius and surface-pressure histories for $\beta = 9$ taken as exact.

β	ε_a (%)	ε_p (%)
3	0.60	1.67
5	0.15	0.47
7	0.03	0.08

sensitive to small differences in time advances or delays among otherwise nearly identical histories, it is not an appropriate error measure for such histories. Hence, tabulated in Table I are normalized peak-value errors in surface-pressure histories, defined by

$$\varepsilon_p(\beta,9) = \frac{Max\{p_\beta\} - Max\{p_9\}}{Max\{p_9\}} \times 100\%,\ 0 \le t \le 10\bar{t}. \quad (46)$$

These errors are approximately three times their bubble-radius counterparts: still quite small.

Second, we compare EE-computed bubble-radius histories for various values of the spatial increment. Histories produced with $\alpha = 3$, $\Delta\hat{t} = 3.16\times10^{-4}$, and $\beta = 7$ for $\Delta\eta = 1.66\times10^{-2}, 0.83\times10^{-2}, 0.415\times10^{-2}$ are visually the same as those in Figure 1. Normalized RMS errors in bubble-radius histories are shown in Table II, with $\Delta\eta = 0.415\times10^{-2}$ playing the normalizing role in this version of Eq. (45). The RMS error for $\Delta\eta = 0.83\times10^{-2}$ is extremely small. Normalized peak-value errors in surface-pressure histories also appear in Table II; the error for $\Delta\eta = 0.83\times10^{-2}$ is also extremely small.

Third, we compare EE-computed bubble-radius histories for various values of the temporal increment. Histories produced with $\alpha = 3$, $\Delta\eta = 0.83\times10^{-2}$, $\beta = 7$ for $\Delta\hat{t} = 6.32\times10^{-4}, 3.16\times10^{-4}, 1.58\times10^{-4}$ are again essentially the same as those in Figure 1. Normalized RMS errors in bubble-radius histories are shown in Table III, with $\Delta\hat{t} = 1.58\times10^{-4}$ playing the normalizing role in this third version of Eq. (45). The normalized RMS error for $\Delta\hat{t} = 3.16\times10^{-4}$ is not extremely small, but is still less than 1%. Normalized peak-value errors in surface-pressure histories also appear in Table III; the error for $\Delta\hat{t} = 3.16\times10^{-4}$ is extremely small.

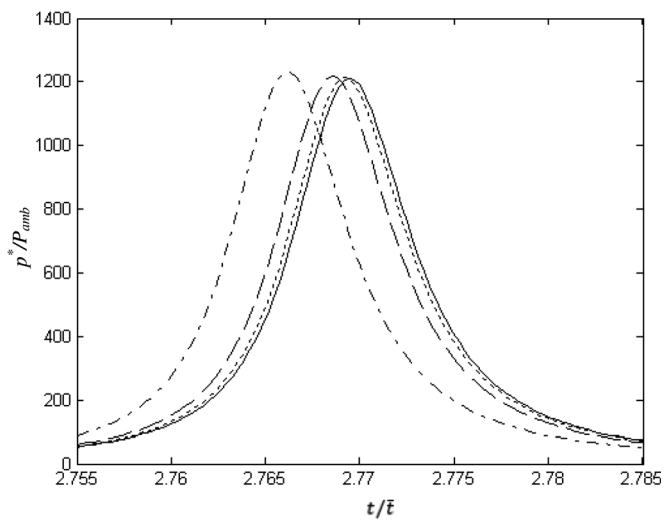

FIG. 2. EE surface-pressure histories computed with $\alpha = 3$, $\Delta\eta = 0.0083$, and $\Delta\hat{t} = 3.16\times10^{-4}$ for $\beta = 3$ (dash-dot), 5 (dash), 7 (dot), and 9 (solid).

TABLE II. Normalized RMS bubble-radius errors and peak-pressure errors during $0 \le t/\bar{t} \le 10$ for $\alpha = 3$, $\Delta\hat{t} = 3.16\times10^{-4}$, $\beta = 7$ and two values of $\Delta\eta$ for EE calculations with the corresponding bubble-radius and surface-pressure histories for $\Delta\eta = 0.415\times10^{-2}$ taken as exact.

$\Delta\eta$	ε_a (%)	ε_p (%)
1.66×10^{-2}	0.20	−0.33
0.83×10^{-2}	0.06	−0.08

From Tables I–III, we conclude that the baseline EE model produces bubble-radius histories and peak-pressure values with normalized RMS and peak-value errors smaller than 1%. Such errors are virtually undetectable in plots such as those in Figure 1.

We are now ready to evaluate numerical results produced by the RP, KK, MLS, GH, and LSS equations [Eqs. (8), (9), (10), (11), and (12)], respectively. Figure 3 compares bubble-radius histories produced by these equations with the benchmark EE history for $\alpha = 2$ during $0 \le t/\bar{t} \le 10$. The RP history exhibits the highest trajectory, the KK, LSS, and EE histories essentially coincide in the middle, and the nearly identical GH and MLS histories exhibit the lowest trajectory. The coincidence of the KK history (external wave effects only), the LSS history (external and internal wave effects), and the EE history implies that wave effects in the bubble gas are negligible.

Figures 4 and 5 show close-up views of bubble-radius histories at the first *bubble minimum* (i.e., the occurrence of a local minimum value of bubble radius) and at the subsequent *bubble maximum* (i.e., the occurrence of a local peak in bubble radius), respectively. We see that the RP history exhibits the lowest bubble minimum and expected absence of energy loss, the nearly coincident KK and LSS histories lie closest to their EE counterparts, and the GH and MLS histories exhibit nearly identical bubble-minimum values and overestimate energy loss to the same degree. For this rather mild collapse, Figure 4 shows that $a_{max}/a_{min} = 5.5$.

Figure 6 displays bubble-surface velocity histories produced by the RP, EE, and MLS equations over $0 \le t/\bar{t} \le 4$. The period during which compressibility effects are noticeable is seen to be about 10% of the elapsed time to the second bubble maximum (with the first bubble maximum at $t = 0$). And within that period, the minimum and maximum

TABLE III. Normalized RMS bubble-radius errors and peak-pressure errors during $0 \le t/\bar{t} \le 10$ for $\alpha = 3$, $\Delta\eta = 0.83\times10^{-2}$, $\beta = 7$ and two values of $\Delta\hat{t}$ for EE calculations with the corresponding bubble-radius and surface-pressure histories for $\Delta\hat{t} = 1.58\times10^{-4}$ taken as exact.

$\Delta\hat{t}$	ε_a (%)	ε_p (%)
6.32×10^{-4}	0.83	−0.10
3.16×10^{-4}	0.53	−0.09

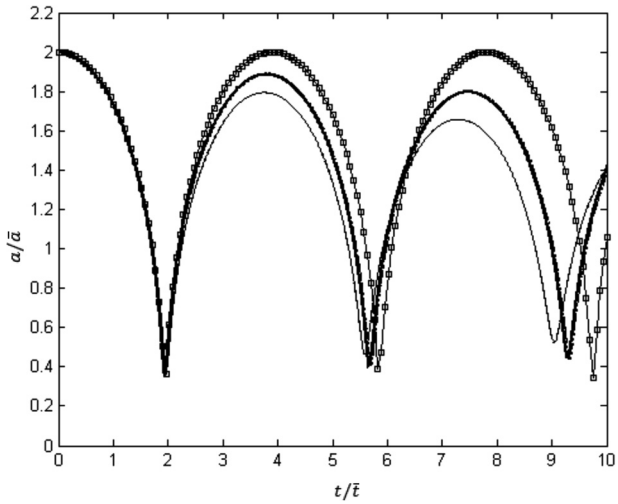

FIG. 3. Bubble-radius histories produced by the RP (connected squares), KK (long dash), LSS (dot), EE (heavy solid), GH (solid), and MLS (short dash) equations for $\alpha = 2$.

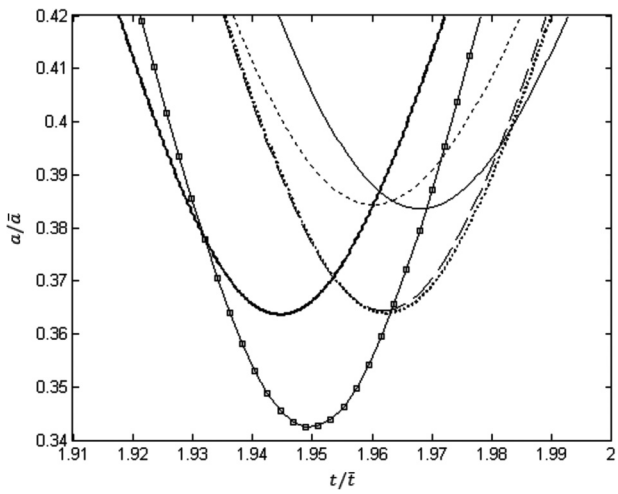

FIG. 4. Bubble-radius histories at the first bubble minimum produced by the RP (connected squares), KK (long dash), LSS (dot), EE (heavy solid), GH (solid), and MLS (short dash) equations for $\alpha = 2$.

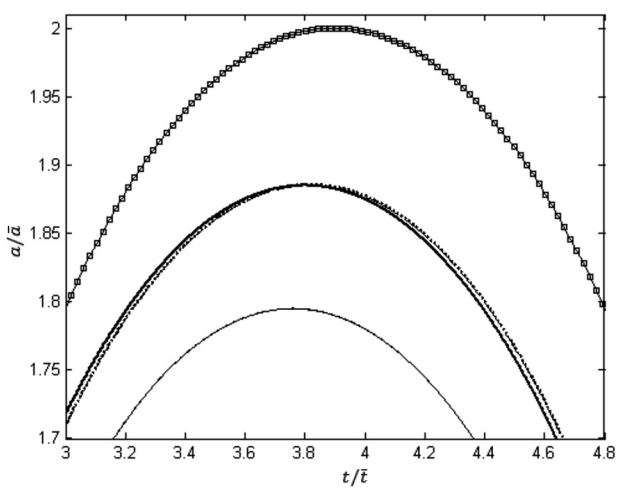

FIG. 5. Bubble-radius histories at the second bubble maximum produced by the RP (connected squares), KK (long dash), LSS (dot), EE (heavy solid), GH (solid), and MLS (short dash) equations for $\alpha = 2$.

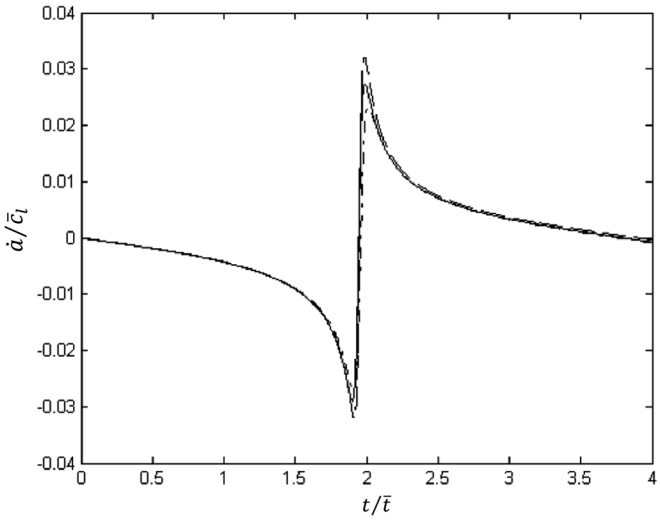

FIG. 6. Bubble-surface velocity histories produced by the RP (dash), EE (solid), and MLS (short dash) equations for $\alpha = 2$.

velocities produced by the equations that most underestimate or overestimate energy loss differ from their EE counterparts by less than 15%. In addition, the figure shows that $|\dot{a}| \ll \bar{c}_\ell$.

Surface-pressure histories during first and second bubble collapse appear in Figures 7 and 8, respectively. As might be expected, the RP peaks are too high, the GH and MLS peaks are too low, and the KK and LSS peaks are just right. The time-of-peak discrepancies are of little importance. Table IV shows normalized bubble-radius RMS errors and normalized peak-pressure errors for the RP, KK, LSS, GH, and MLS equations when $\alpha = 2$. The values support the results exhibited in Figures 3–5, 7, and 8.

Figure 9 compares the reduced-equation bubble-radius histories with the benchmark EE history for $\alpha = 3$ during $0 \le t/\bar{t} \le 15$. Here too, the RP history exhibits the highest trajectory, the KK, LSS, and EE histories essentially coincide in the middle, and the nearly identical GH and MLS histories exhibit the lowest trajectory. The coincidence of the

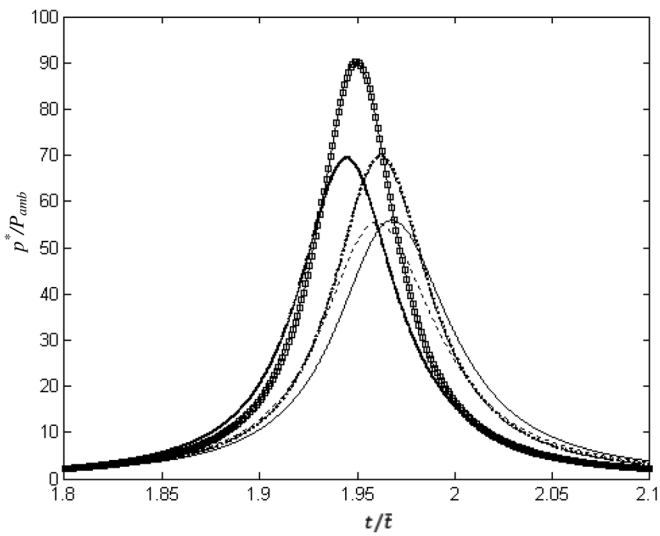

FIG. 7. First pressure pulses produced by the RP (connected squares), KK (long dash), LSS (dot), EE (heavy solid), GH (solid), and MLS (short dash) equations for $\alpha = 2$.

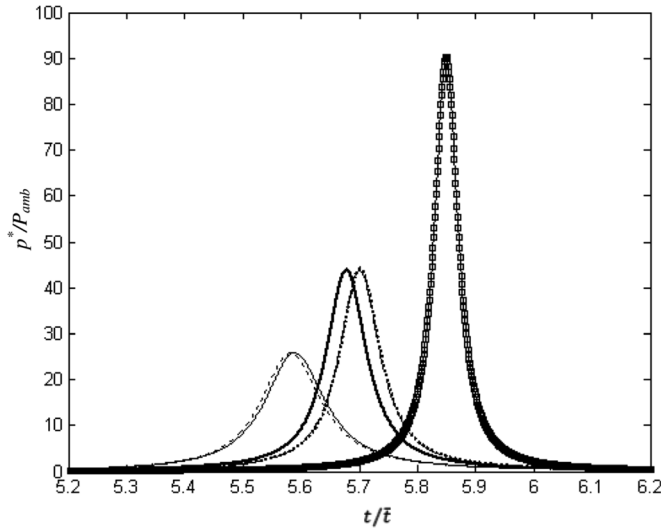

FIG. 8. Second pressure pulses produced by the RP (connected squares), KK (long dash), LSS (dot), EE (heavy solid), GH (solid), and MLS (short dash) equations for $\alpha = 2$.

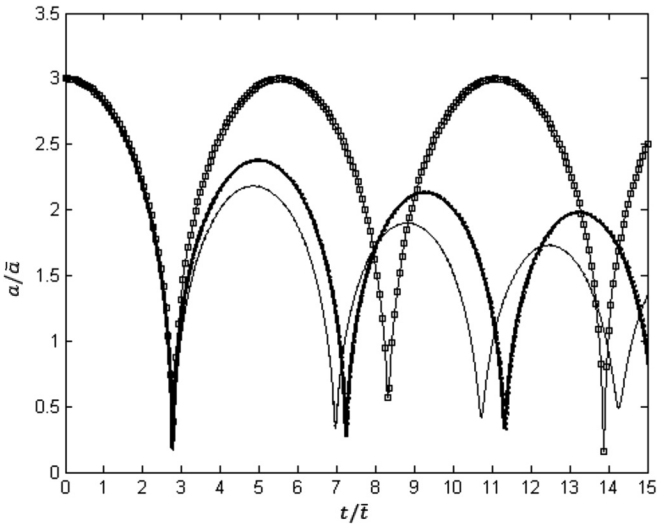

FIG. 9. Bubble-radius histories produced by the RP (connected squares), KK (long dash), LSS (dot), EE (heavy solid), GH (solid), and MLS (short dash) equations for $\alpha = 3$.

KK, LSS, and EE histories again implies that wave effects in the bubble gas are negligible. Energy loss, as indicated by steady decreases in bubble maxima relative to the initial maximum, is substantially greater for $\alpha = 3$ than for $\alpha = 2$. Figures for $\alpha = 3$ that correspond to Figures 4–8 for $\alpha = 2$ exhibit similar behavior, yielding $a_{max}/a_{min} = 16.5$.

Surface-pressure histories during first bubble collapse appear in Figure 10. The RP peak is far too high, the LSS peak is too high, the GH and MLS peaks are too low, and the KK peak is only slightly higher than the EE peak. Again, the time-of-peak discrepancies are of minor importance. The results are summarized in Table V, which shows discrepancies considerably greater than those seen in Table IV.

Figure 11 compares the reduced-equation bubble-radius histories with the benchmark EE history for $\alpha = 4$ during $0 \le t/\bar{t} \le 20$. The discussion of the previous paragraph holds in this case also with energy loss for $\alpha = 4$ being substantially greater than that for $\alpha = 3$, as now $a_{max}/a_{min} = 30.5$. Surface-pressure histories during first bubble collapse appear in Figure 12. The RP peak is out of sight, the LSS peak is far too high, the KK peak is too high, and the GH and MLS peaks are too low. The results are summarized in Table VI.

X. ABSENCE OF SHOCKWAVES

The high velocity attained by the bubble surface during a collapse event raises the possibility of shockwave generation. Table VII shows maximum values for the ratio of bubble-surface-velocity magnitude to sound speed in the bubble gas and in the surrounding liquid. While the ratios for the liquid are all substantially less than unity, those for the bubble gas are not when $\alpha = 3$ or $\alpha = 4$.

But a shockwave builds slowly unless the physical properties of the medium change substantially along the travel path, which is not the case here, as the pressure field in the bubble is nearly constant. This is seen in the curves of Figure 13, which constitute five pressure snapshots inside the bubble during the first pulse duration $2.76 \le t/\bar{t} \le 2.78$ (see Figure 10). The maximum decrease from the value at the bubble center, which occurs at the first bubble minimum (Snapshot 3), is 9%. One might argue that algorithmic damping in the EE computations could have suppressed the formation of shockwaves. Such damping, however, is a function of discretization refinement, which shows little effect in Tables II and III.

TABLE IV. Normalized RMS bubble-radius errors and peak-pressure errors during $0 \le t/\bar{t} \le 10$ for $\alpha = 2$.

Equation	ε_a (%)	ε_p (%)
RP	29.4	29.9
KK	1.2	−0.0
LSS	2.0	0.6
GH	24.9	−19.4
MLS	24.8	−20.1

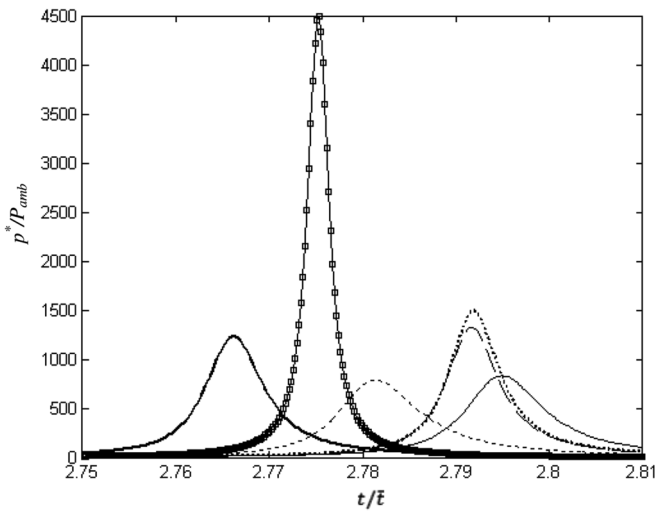

FIG. 10. First pressure pulses produced by the RP (connected squares), KK (long dash), LSS (dot), EE (heavy solid), GH (solid), and MLS (short dash) equations for $\alpha = 3$.

TABLE V. Normalized RMS bubble-radius errors and peak-pressure errors during $0 \le t/\bar{t} \le 15$ for $\alpha = 3$.

Equation	ε_a (%)	ε_p (%)
RP	63.7	265.3
KK	3.7	7.5
LSS	4.1	20.9
GH	34.0	−32.7
MLS	33.7	−36.3

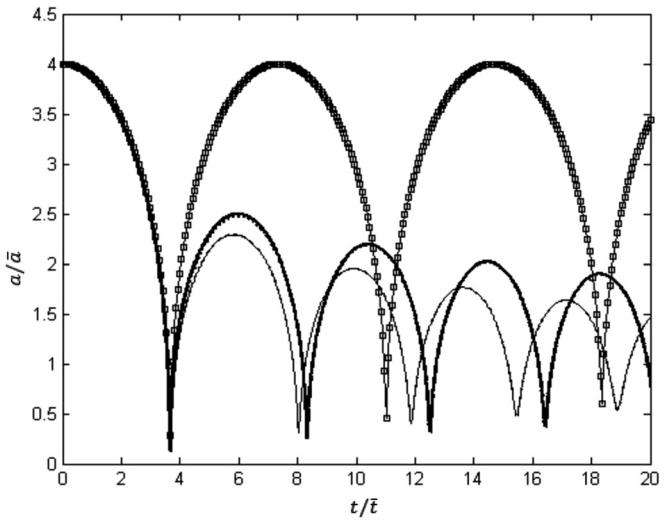

FIG. 11. Bubble-radius histories produced by the RP (connected squares), KK (long dash), LSS (dot), EE (heavy solid), GH (solid), and MLS (short dash) equations for $\alpha = 4$.

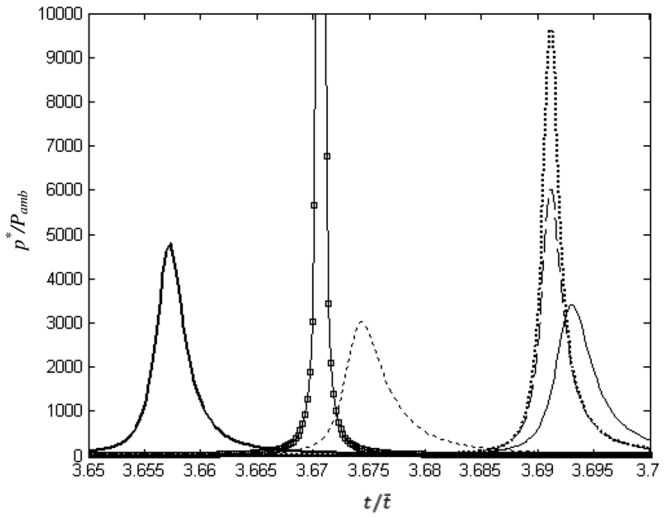

FIG. 12. First pressure pulses produced by the RP (connected squares), KK (long dash), LSS (dot), EE (heavy solid), GH (solid), and MLS (short dash) equations for $\alpha = 4$.

TABLE VI. Normalized RMS bubble-radius errors and peak-pressure errors during $0 \le t/\bar{t} \le 20$ for $\alpha = 4$.

Equation	ε_a (%)	ε_p (%)
RP	84.0	1297.5
KK	6.6	25.5
LSS	8.5	102.5
GH	30.9	−28.5
MLS	30.4	−36.9

TABLE VII. Maximum values of the ratio of bubble-surface-velocity magnitude to sound speed in the gas and in the liquid.

α	$[\lvert\dot{a}(t)\rvert/c_g(a,t)]_{max}$	$[\lvert\dot{a}(t)\rvert/\bar{c}_\ell]_{max}$
2	0.1795	0.0295
3	1.0721	0.1359
4	2.8001	0.2987

The behavior seen in Figure 13 is predicted by a perturbation analysis of the pressure-velocity equations for the gas, Eqs. (18). We begin the analysis by selecting $\bar{\rho}_\ell$, P_{amb}, and $\bar{a}$ as normalization parameters, which leads to the nondimensional variables $\hat{r} = r/\bar{a}$, $\hat{t} = (\sqrt{P_{amb}/\bar{\rho}_\ell}/\bar{a})t$, $\hat{p} = p_g^*/P_{amb}$, and $\hat{u} = u_g/\sqrt{P_{amb}/\bar{\rho}_\ell}$. Introducing these variables into Eqs. (18), we obtain

$$\frac{\partial \hat{p}}{\partial \hat{r}} = -\varepsilon(\hat{p}+1)^{1/\gamma}\left(\frac{\partial \hat{u}}{\partial \hat{t}} + \hat{u}\frac{\partial \hat{u}}{\partial \hat{r}}\right),$$
$$\frac{\partial \hat{u}}{\partial \hat{r}} + \frac{2}{\hat{r}}\hat{u} = -\frac{1}{\gamma(\hat{p}+1)}\left(\frac{\partial \hat{p}}{\partial \hat{t}} + \hat{u}\frac{\partial \hat{p}}{\partial \hat{r}}\right), \tag{47}$$

where $\varepsilon = \bar{\rho}_g/\bar{\rho}_\ell$ is the perturbation parameter. Thus, we expand $\hat{p}(\hat{r},\hat{t})$ and $\hat{u}(\hat{r},\hat{t})$ as

$$\hat{p}(\hat{r},\hat{t}) = \hat{p}_0(\hat{r},\hat{t}) + \varepsilon\hat{p}_1(\hat{r},\hat{t}) + \varepsilon^2\hat{p}_2(\hat{r},\hat{t}) + \ldots,$$
$$\hat{u}(\hat{r},\hat{t}) = \hat{u}_0(\hat{r},\hat{t}) + \varepsilon\hat{u}_1(\hat{r},\hat{t}) + \varepsilon^2\hat{u}_2(\hat{r},\hat{t}) + \ldots. \tag{48}$$

Introducing Eqs. (48) into Eqs. (47) and dropping all terms involving powers of ε higher than zero, we obtain $\partial\hat{p}_0/\partial\hat{r} = 0$ and $\partial\hat{u}_0/\partial\hat{r} + (2/\hat{r})\hat{u}_0 = (-\partial\hat{p}_0/\partial\hat{t})/\gamma(\hat{p}_0+1)$. The solutions to these equations are $\hat{p}_0(\hat{r},\hat{t}) = \hat{p}_0(\hat{t})$ and $\hat{u}_0(\hat{r},\hat{t}) = \hat{U}_0(\hat{t})\hat{r}$, in which

$$\hat{U}_0(\hat{t}) = -\hat{\dot{P}}_0(\hat{t})/3\gamma[\hat{P}_0(\hat{t}) + 1], \tag{49}$$

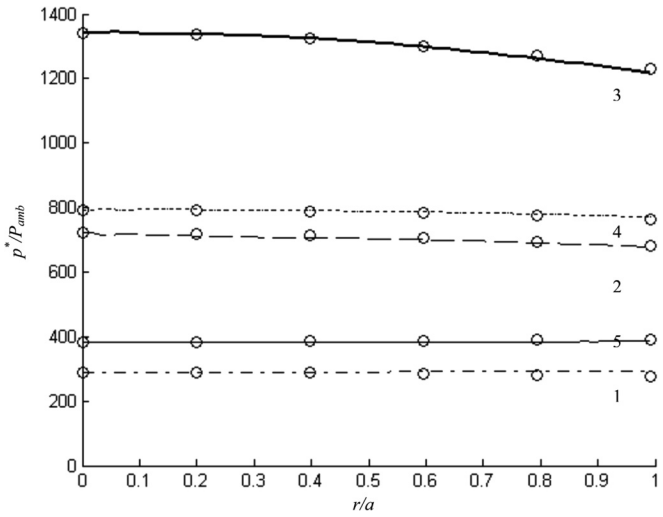

FIG. 13. Snapshots of $p^*(r,t)/P_{amb}$ for $0 \le r/a \le 1$ at (1) $t/\bar{t} = 2.763$, (2) $t/\bar{t} = 2.766$, (3) $t/\bar{t} = 2.769$, (4) $t/\bar{t} = 2.772$, (5) $t/\bar{t} = 2.775$ for $\alpha = 3$; circles are perturbation-analysis values.

where $\hat{\dot{P}}_0(\hat{t}) = d\hat{P}_0/d\hat{t}$. These solutions are, of course, the bubble-gas fields associated with the RP and KK equations. Again introducing Eqs. (48) into Eqs. (47) but dropping all terms involving powers of ε higher than one, we get a more complicated pair of equations, which yield $\hat{p}_1(\hat{r},\hat{t}) = \hat{P}_1(\hat{t})\hat{r}^2$ and $\hat{u}_1(\hat{r},\hat{t}) = \hat{U}_1(\hat{t})\hat{r}^3$, where

$$\begin{aligned}\hat{P}_1(\hat{t}) &= -\frac{1}{2}[\hat{P}_0(\hat{t})+1]^{1/\gamma}[\hat{\dot{U}}_0(\hat{t}) + \hat{U}_0^2(\hat{t})],\\ \hat{U}_1(\hat{t}) &= -[\hat{\dot{P}}_1 + (3\gamma+2)\hat{U}_0(\hat{t})\hat{P}_1(\hat{t})]/5\gamma[\hat{P}_0(\hat{t})+1].\end{aligned} \tag{50}$$

Thus, it is clear that Eqs. (48) take the form

$$\begin{aligned}\hat{p}(\hat{r},\hat{t}) &= \hat{P}_0(\hat{t}) + \varepsilon\hat{P}_1(\hat{t})\hat{r}^2 + \varepsilon^2\hat{P}_2(\hat{t})\hat{r}^4 + ...,\\ \hat{u}(\hat{r},\hat{t}) &= \hat{U}_0(\hat{t})\hat{r} + \varepsilon\hat{U}_1(\hat{t})\hat{r}^3 + \varepsilon^2\hat{U}_2(\hat{t})\hat{r}^5 + ...\end{aligned} \tag{51}$$

To check this analysis, we computed $\hat{P}_0(\hat{t}) = P_{amb}^{-1}p_g^*(0,t)$, $\hat{\dot{P}}_0(\hat{t}) \approx [\hat{P}_0(\hat{t}+\Delta\hat{t}) - \hat{P}_0(\hat{t}-\Delta\hat{t})]/2\Delta\hat{t}$, $\hat{U}_0(\hat{t})$ from Eq. (49), $\hat{\dot{U}}_0(\hat{t}) \approx [\hat{U}_0(\hat{t}+\Delta\hat{t}) - \hat{U}_0(\hat{t}-\Delta\hat{t})]/2\Delta\hat{t}$, $\hat{P}_1(\hat{t})$ from the first of Eqs. (50), and, finally, $\hat{p}_{II}(\hat{r},\hat{t}) = \hat{P}_0(\hat{t}) + \varepsilon\hat{P}_1(\hat{t})\hat{r}^2$ for the snapshots of Figure 13. The results, which are shown as circles in the figure, agree closely with the EE-computed snapshots. Hence, one expects to see gradual heaving in the snapshots rather than wave profiles propagating along the radius. A snapshot for $\alpha = 4$ at the time of the first bubble minimum is as smooth as snapshot 3 in Figure 13, even though the maximum decrease in pressure from the value at the bubble center is 19% rather than 9%. Also, the agreement between predictions from the perturbation analysis and the EE-computed snapshots for $\alpha = 4$ is comparable to that seen in Figure 13 for $\alpha = 3$.

XI. ENERGY

The impressive accuracy of the DAA boundary seen in Table I facilitates an examination of energy flow in the benchmark problem. We begin by determining the initial potential energy in the liquid and the gas. The potential energy in the liquid is equal to the work done on it as a spherical void expands slowly against the ambient pressure from zero volume to the initial volume V_0. This work produces, with $V_0 = \frac{4}{3}\pi(\alpha\bar{a})^3$,

$$U_\ell(0) = \int_0^{V_0} pdV = P_{amb}\int_0^{V_0} dV = \frac{4}{3}\pi P_{amb}(\alpha\bar{a})^3. \tag{52}$$

The potential energy in the gas is produced by slow, adiabatic compression from infinite volume (zero potential energy) to volume V_0. From the adiabatic relation $pV^\gamma = P_{amb}\bar{V}^\gamma$, where $\bar{V}$ is the bubble volume under equilibrium conditions, we find, with $\bar{V} = \frac{4}{3}\pi\bar{a}^3$ and $V_0 = \frac{4}{3}\pi(\alpha\bar{a})^3$,

$$\begin{aligned}U_g(0) &= \int_\infty^{V_0} p\cdot(-dV) = -P_{amb}\bar{V}^\gamma\int_\infty^{V_0} V^{-\gamma}dV\\ &= \frac{4}{3}\pi P_{amb}(\alpha\bar{a})^3\frac{\alpha^{-3\gamma}}{\gamma-1}.\end{aligned} \tag{53}$$

For $t > 0$, we adopt a dynamic model that consists of the gas in the bubble and a DAA boundary right on the bubble's surface; there is no liquid in this model. We employ the $\hat{p}_0$ and $\hat{u}_0$ gas models of the previous section, so that the pressure and velocity fields in the bubble are given by $p^*(r,t) = p^*(a,t)$ and $u(r,t) = [\dot{a}(t)/a(t)]r$, $0 \le r \le a(t)$. These yield the following approximations for the kinetic and potential energies in the gas:

$$\begin{aligned}T_g(t) &\approx \frac{1}{2}\rho_g(t)\int_0^{a(t)} u^2(r,t)\cdot 4\pi r^2 dr = \frac{2}{5}\pi\rho_g(t)a^3(t)\dot{a}^2(t),\\ U_g(t) &\approx \frac{4}{3}\pi P_{amb}a^3(t)\frac{1}{\gamma-1}[\bar{a}/a(t)]^{3\gamma},\end{aligned} \tag{54}$$

the latter produced by Eq. (53) with V_0 replaced by $V(t) = \frac{4}{3}\pi a^3(t)$.

Now the power transmitted into the computational boundary is given by

$$\prod_b(t) = 4\pi a^2(t)[P_{amb} + p^*(a,t)]\dot{a}(t). \tag{55}$$

This equation pertains to a Lagrangian frame of reference, whereas the DAA_1 equation, Eq. (22), pertains to an Eulerian frame, so we follow Geers and Hunter (2002) to express the latter equation at the bubble surface in a Lagrangian frame. The result is the KK equation, Eq. (4), which we rearrange to obtain

$$\begin{aligned}p^*(a,t)\dot{a}(t) = \bar{\rho}_\ell\Bigg[&\frac{1-\dot{a}(t)/\bar{c}_\ell}{1+\dot{a}(t)/\bar{c}_\ell}a(t)\dot{a}(t)\ddot{a}(t)\\ &+\frac{3}{2}\frac{1-\frac{1}{3}\dot{a}(t)/\bar{c}_\ell}{1+\dot{a}(t)/\bar{c}_\ell}\dot{a}^3(t)\Bigg] - \frac{a(t)\dot{a}(t)/\bar{c}_1}{1+\dot{a}(t)/\bar{c}_1}\dot{p}^*(a,t).\end{aligned} \tag{56}$$

Because Eq. (56) is accurate only through $O(\dot{a}/\bar{c}_\ell)$, we can divide the denominator $1+\dot{a}(t)/\bar{c}_\ell$ into the three numerators, drop terms of $O([\dot{a}/\bar{c}_\ell]^2)$ and higher, and introduce the result into the integral of Eq. (55) to obtain, through $O(\dot{a}/\bar{c}_\ell)$,

$$\begin{aligned}E_b(t) = const. &+ 4\pi P_{amb}\int_0^t a^2(t')\dot{a}(t')dt'\\ &+ 4\pi\bar{\rho}_\ell\int_0^t\left[a^3(t')\dot{a}(t')\ddot{a}(t') + \frac{3}{2}a^2(t')\dot{a}^3(t')\right]dt'\\ &- 8\pi\frac{\bar{\rho}_\ell}{\bar{c}_\ell}\int_0^t[a^3(t')\dot{a}^2(t')\ddot{a}(t') + a^2(t')\dot{a}^4(t')]dt'\\ &- \frac{4\pi}{\bar{c}_\ell}\int_0^t[1-\dot{a}(t')/\bar{c}_\ell]a^3(t')\dot{a}(t')\dot{p}^*(a,t')dt'.\end{aligned} \tag{57}$$

But $a^2\dot{a} = \frac{1}{3}\frac{d}{dt}(a^3)$, $a^3\dot{a}\ddot{a} + \frac{3}{2}a^2\dot{a}^3 = \frac{1}{2}\frac{d}{dt}(a^3\dot{a}^2)$, and $a^3\dot{a}^2\ddot{a} + a^2\dot{a}^4 = \frac{1}{3}\frac{d}{dt}(a^3\dot{a}^3)$, so Eq. (57) becomes, with the condition that $E_b(0) = U_\ell(0)$,

$$E_b(t) = T_\ell(t) + U_\ell(t) + E_r(t), \tag{58}$$

where

$$T_\ell(t) = \frac{1}{2}\left[1 - \frac{4}{3}\dot{a}(t)/\bar{c}_\ell\right] 4\pi\bar{\rho}_\ell a^3(t)\dot{a}^2(t),$$
$$U_\ell(t) = \frac{4}{3}\pi P_{amb} a^3(t), \tag{59}$$
$$E_r(t) = -\frac{4\pi}{\bar{c}_\ell}\int_0^t [1 - \dot{a}(t)/\bar{c}_\ell] a^3(t')\dot{a}(t')\dot{p}^*(a,t')dt'.$$

$T_l(t)$ is the kinetic energy of an incompressible liquid surrounding the bubble, but with the added mass reduced by the multiplier $1 - \frac{4}{3}\dot{a}(t)/\bar{c}_\ell$. $U_l(t)$ is the potential energy in the liquid due to bubble expansion against the ambient pressure. $E_r(t)$ is the radiated energy, as the integrand does not produce an exact differential. The added-mass multiplier goes to unity and $E_r(t)$ vanishes as $\bar{c}_\ell \to \infty$, i.e., in the limit of incompressible flow. Because system energy is fully contained within the bubble gas and the DAA boundary, we can write

$$E_r(t) = U_\ell(0) + U_g(0) - [T_\ell(t) + T_g(t) + U_\ell(t) + U_g(t)]. \tag{60}$$

Even though most of the energy is radiated in the vicinity of bubble minima, it is more informative to calculate E_r at the bubble maxima, when T_l and T_g both vanish. With t_{Mj} as the time of the jth bubble maximum and $\alpha_j = a(t_{Mj})/\bar{a}$, the total energy at that time is

$$U(t_{Mj}) = U_\ell(t_{Mj}) + U_g(t_{Mj}) = \frac{4}{3}\pi P_{amb}[\alpha_j\bar{a}]^3\left(1 + \frac{\alpha_j^{-3\gamma}}{\gamma - 1}\right), \tag{61}$$

where $t_{M1} = 0$, $\alpha_1 = \alpha$ and $\alpha_j < \alpha$, $j \geq 2$. Thus, from Eqs. (60) and (61), the ratio of the radiated energy at the time t_{Mj} to the initial energy is

$$\frac{E_r(t_{Mj})}{U(0)} = 1 - \left(\frac{\alpha_j}{\alpha}\right)^3 \frac{\gamma - 1 + \alpha_j^{-3\gamma}}{\gamma - 1 + \alpha^{-3\gamma}}. \tag{62}$$

Values of this ratio for $\alpha = 2$, 3, and 4 obtained from the essentially coincident KK, LSS, and EE histories in Figures 3, 9, and 11 appear in Table VIII. We see that the amount of energy radiated increases rapidly with α and is most pronounced at the first bubble minimum.

Finally, we compare the kinetic energy in the gas with that in the liquid. From the first of Eqs. (54) and (59),

$$\frac{T_g(t)}{T_\ell(t)} = \frac{1}{5}\frac{\rho_g(t)/\bar{\rho}_\ell}{1 - \frac{4}{3}\dot{a}(t)/\bar{c}_\ell}. \tag{63}$$

TABLE VIII. Normalized bubble energy radiated by the times of the second and third bubble maxima for three values of α.

α	$E_r(t_{M2})/U(0)$	$E_r(t_{M3})/U(0)$
2	0.13	0.22
3	0.48	0.62
4	0.75	0.82

Because $\rho_g(t) \ll \bar{\rho}_\ell$ and $(\dot{a}(t)/\bar{c}_\ell)^2 \ll 1$ at all times, $T_g(t)$ is always much smaller than $T_l(t)$.

XII. CONCLUSION

To address observed discrepancies between experimentally measured bubble-radius histories and histories generated by reduced bubble equations that do not account for wave effects inside the bubble, modelers have derived Eqs. (5)–(7), which incorporate such effects. As reported in Moss *et al.* (2000) and Geers and Hunter (2002), the new equations produced bubble histories that predicted more accurately the energy loss observed in experimental data. However, such loss could have been the result of other natural phenomena that were not treated in the reduced bubble equations.

In order to provide an unambiguous examination, we have formulated a benchmark problem based on adiabatic conditions and Euler equations for both the surrounding liquid and the bubble gas, thereby excluding all non-acoustic energy-loss phenomena. The benchmark problem was designed to maintain a sharp boundary between the liquid and the gas, and incorporated initial conditions associated with purely incompressible flow. Convergence of the numerical model to better than a 99% accuracy level was demonstrated. Bubble-radius, surface-velocity, and surface-pressure histories produced by the RP equation (which incorporates no wave effects at all), the KK equation (which incorporates wave effects only in the external liquid), and the MLS, GH, and LSS equations (which incorporate wave effects in both the external liquid and the internal gas) were compared with corresponding EE-calculated benchmark histories in Figures 3–12 and Tables IV-VI.

The principal conclusion that emerges from the comparisons is that, although wave effects in the external liquid are important, wave effects in the internal gas are of no consequence. Hence, observed discrepancies between the predictions of KK-type models and experimental data must be caused by non-acoustic phenomena.

Another conclusion emerging from this study is that the pressure field in the gas is weakly dependent on radius, even at bubble collapse. Neither propagating acoustic waves nor shockwaves are discernable in pressure snapshots calculated at times at and around the time of the first bubble collapse. This outcome is predicted by a perturbation analysis of the pressure-velocity equations for the gas.

A third conclusion is that the computational boundary based on the first-order DAA_1 is highly effective, providing an accuracy level of about 99% even when the boundary is located on the surface of the bubble. This is due to the fact that DAA_1 is exact for small-motion dilation of a spherical surface. When located on the moving surface of a dilating bubble with spatially uniform internal pressure, it produces the KK equation. Placement of the DAA boundary directly on the bubble surface admitted a simple analysis of energy flow in the gas and liquid. The analysis showed large acoustic radiation losses during the first bubble collapse for $\alpha = 3$ and $\alpha = 4$.

The benchmark model presented in this paper can be extended to include other phenomena, those associated with non-adiabatic conditions in particular. It is, however, limited

to pure bubble dilation. For more general (and complex) bubble motion, an attractive modeling approach would consist of finite-element semi-discretization of the bubble interior coupled with a boundary-element treatment of the surrounding liquid. This approach has, in fact, been used by several researchers, with the boundary-element treatment based on incompressible flow of the liquid [for recent examples, see Wang *et al*. (2003); Klaseboer *et al*. (2005)]. However, the poor performance of the RP equation exhibited in this and previous studies has demonstrated that the incompressible-flow treatment is not a good one. A better alternative would be to base the boundary-element treatment on the external DAA_1. Such a treatment would not be as accurate as that seen here for pure dilation, but it would be substantially better than the incompressible-flow treatment.

Besant, W. H., *Hydrostatics and Hydromechanics* (Bell, London, 1859), pp. 331–333.

Brenner, P. M., Hilgenfeldt, S., and Lohse, D., "Single-bubble sonoluminescence," Rev. Mod. Phys. **74**, 425–483 (2002).

Fletcher, C. A. J., *Computational Techniques for Fluid Dynamics*, (Springer-Verlag, Berlin, 1988), Vol. 2, pp. 331–333.

Geers, T. L. and Hunter, K. S., "An integrated wave-effects model for an underwater explosion bubble," J. Acoust. Soc. Am. **111**, 1584–1601 (2002).

Geers, T. L. and Zhang, P., "Doubly asymptotic approximations for submerged structures with internal fluid volumes," J. Appl. Mech. **61**, 893–906 (1994).

Gilmore, F. R., "The growth or collapse of a spherical bubble in a viscous compressible liquid," Hydrodynamics Laboratory, California Institute of Technology, Pasadena, Report No. 26–4, 1952.

Herring, C., "Theory of the pulsations of the gas bubble produced by an underwater explosion," in *Underwater Explosion Research* (Office of Naval Research, Washington, 1950), pp. 35–131 (1941).

Keller, J. B. and Kolodner, I. I., "Damping of underwater explosion bubble oscillations," J. Appl. Phys. **27**, 1152–1161 (1956).

Keller, J. B. and Miksis, M. J., "Bubble oscillations of large amplitude," J. Acoust. Soc. Am. **68**, 628–633 (1980).

Kirkwood, J. G. and Bethe, H., "The pressure wave produced by an underwater explosion I. (OSRD No. 588)," in *Shock and Detonation Waves*, edited by W. W. Wood (Gordon and Breach, NY, 1967), pp. 1–34 (1942).

Klaseboer, E., Khoo, B. C., and Hung, K. C., "Dynamics of an oscillating bubble near a floating structure," J. Fluids Struct. **21**, 395–412 (2005).

Lamb, H., "The early stages of a submarine explosion," Philos. Mag. **45(6)**, 257–265 (1923).

Lamb, H., *Hydrodynamics* (Dover, Mineola, NY, 1932).

Leighton, T. G., *The Acoustic Bubble* (Academic, New York, 1994).

Lin, H., Storey, B. D., and Szeri, A. J., "Inertially driven inhomogeneities in violently collapsing bubbles: The validity of the Rayleigh-Plesset equation," J. Fluid Mech. **452**, 145–162 (2002).

Löfstedt, R., Barber, B. P., and Putterman, S. J., "Toward a hydrodynamic theory of sonoluminescence," Phys. Fluids A **5**, 2911–2928 (1993).

Moss, W. C., Levatin, J. L., and Szeri, A. J., "A new damping mechanism in strongly collapsing bubbles," Proc. R. Soc London, Ser. A **456**, 2983–2994 (2000).

Pierce, A. D., *Acoustics* (Acoustical Society of America, 1989), pp. 177–178.

Prosperetti, A. and Lezzi, A., "Bubble dynamics in a compressible liquid I. First-order theory," J. Fluid Mech. **168**, 457–478 (1986).

Lord Rayleigh (J. W. Strutt), "The pressure developed in a liquid on the collapse of a spherical cavity," Philos. Mag. **34**, 94–98 (1987).

Wang, C., Khoo, B. C., and Yeo, K. S., "Elastic mesh technique for 3D BIM simulation with an application to underwater explosion bubble dynamics," Comput. Fluids **32**, 1195–1212 (2003).

Young, F. R., *Cavitation* (Mc-Graw-Hill, London, 1989), Chap. 2.

Young, F. R., *Sonoluminescence* (CRC, Boca Raton, 2005), Chap. 5.